
# Quantitative Mapping of Triacylglycerol Chain Length and Saturation Using Broadband CARS Microscopy

Biophysical Journal
Article

Biophysical Society

# Quantitative Mapping of Triacylglycerol Chain Length and Saturation Using Broadband CARS Microscopy

Alexandra Paul,[1,2] Yujen Wang,[2,3] Cecilia Brännmark,[4] Sachin Kumar,[2,3] Mischa Bonn,[2] and Sapun H. Parekh[2,3,*]
[1]Division of Chemical Biology, Department of Biology and Biological Engineering, Chalmers University of Technology, Gothenburg, Sweden; [2]Department of Molecular Spectroscopy, Max Planck Institute for Polymer Research, Mainz, Germany; [3]Department of Biomedical Engineering, The University of Texas at Austin, Austin, Texas; and [4]Institute of Neuroscience and Physiology, Unit of Metabolic Physiology, Department of Physiology, Sahlgrenska Academy at the University of Gothenburg, Gothenburg, Sweden

ABSTRACT Lipid droplets (LDs), present in many cell types, are highly dynamic organelles that store neutral lipids, primarily triacylglycerols (TAGs). With the discovery of new LD functions (e.g., in immune response, protein clearage, and occurrence with disease), new methods to study LD chemical composition in situ are necessary. We present an approach for in situ, quantitative TAG analysis using label-free, coherent Raman microscopy that allows deciphering LD TAG composition in different biochemically complex samples with submicrometer spatial resolution. Employing a set of standard TAGs, we generate a spectral training matrix capturing the variation caused in Raman-like spectra by TAG backbone, chain length, and number of double bonds per chain, as well as the presence of proteins or other diluting molecules. Comparing our fitting approach to gas chromatography measurements for mixtures of standard TAGs and food oils, we find the root mean-square error for the prediction of TAG chemistry to be 0.69 $CH_2$ and 0.15 #C=C. When progressing to more complex samples such as oil emulsions and LDs in various eukaryotic cells, we find good agreement with bulk gas chromatography measurements. For differentiated adipocytes, we find a significant increase in the number of double bonds in small LDs (below 2 $\mu$m in diameter) compared to large LDs (above 2 $\mu$m in diameter). Coupled with a relatively limited sample preparation requirement, this approach should enable rapid and accurate TAG LD analysis for a variety of cell biology and technological applications.

## INTRODUCTION

Many cell types use lipid droplets (LDs) as efficient storage depots to provide energy in times of scarce nutritional supplies. To build up these depots, free fatty acids, either taken up or synthesized by cells, are esterified into neutral lipids, such as triacylglycerol (TAG) by acyl transferase enzymes. These hydrophobic TAG molecules form droplets together with other esterified molecules inside the cytosol, and the droplets are covered by an emulsifying monolayer of phospholipids (1,2). Additionally, various proteins are associated with LDs (e.g., the perilipin proteins in mammals or oleosins in plants), which can have various functions from anchoring lipases to serving as scaffolds for signaling molecules (2). LDs have been found across many different species, with the consensus being that LDs contain mostly TAGs, sterol esters, and, to a lesser extent, diacylglycerol. The ratios between these molecular species can vary vastly between different cell types and potentially for the same cell in different cellular states (e.g., under disease conditions (3,4)). In mammals, there is a specific cell type, adipocytes, designated to acquit lipotoxicity and store TAGs for energy usage. Outside of adipocytes, LDs also appear in many other mammalian tissues, especially when the mammal is exposed to high levels of fatty acid intake; such ectopic lipid accumulation has been identified to cause dysfunction and death of the lipid-laden cells. One example is in pancreatic $\beta$-cells in which excess lipid accumulation has been found to interfere with insulin secretion (5) and also lead to apoptosis (6).

Similar to mammals, prokaryotic yeast have lipid accumulations, which are largely full of TAGs, that allow cells to deal with lipotoxicity (7). TAGs in yeast can also be a desired product in the search for the replacement of plant-based resources such as cocoa butter (8). In addition to cocoa seeds, many other plants such as soy and olive seeds store TAGs in LD analogs called oil bodies (3), which are similarly coated with amphipathic lipids and regulatory proteins (9).

*Submitted November 5, 2018, and accepted for publication April 25, 2019.*
*Correspondence: sparekh@utexas.edu
Editor: Stephen Evans.
https://doi.org/10.1016/j.bpj.2019.04.036

Over the last 15 years, it has become clear that LDs in a single organism can be divided into different subpopulations according to lipid composition and proteins associated with the LD phospholipid coating (10–12). Moreover, the size and location of the droplets differ between cell types and organisms. A clear example is, again, mammalian white adipocytes in which a large, central LD fills almost all of the cellular volume (13), whereas in muscle myocytes for example, LDs appear smaller and dispersed in the cells (14–16). This same appearance of small LDs is also observed for *Drosophila* fat bodies (17,18) as well as in yeast (19,20) and plant cells (21). In addition to different size, LD composition can also differ among individual cells (22) and even within single cells (23). Importantly, fatty acid composition, particularly carbon saturation level found in ectopic LDs in skeletal muscle and chain length of free fatty acids in the blood, is known to correlate with increased insulin resistance (24) and stimulation of insulin secretion (25), respectively. Moreover, exposing cultured cells to saturated fatty acids is known to be cytotoxic, whereas an equivalent concentration of unsaturated fatty acids can be relatively benign (26). Because fatty acids in cells are eventually stored in LDs, there is a need to quantify the lipid chemistry at the individual LD level in cells.

Traditional approaches for the characterization of lipid chemistry in cells or tissues involve the extraction of all lipids followed by derivatization and analysis with gas chromatography mass spectrometry (GC-MS) (27). The location of cellular LDs can be determined within cells using microscopy via fluorescence markers (28,29) or label-free vibrational imaging such as coherent Raman scattering (CRS) microscopy (30–32). To achieve spatial information coupled to chemical structures, three main methods have emerged during the recent years: 1) matrix-assisted laser desorption/ionization mass spectrometry imaging (MALDI-MSI), 2) magnetic resonance imaging, and 3) hyperspectral Raman or coherent anti-Stokes Raman scattering (CARS) microscopy. MALDI-MSI has been used to identify lipid species with high accuracy and $>1.4$ $\mu$m spatial resolution in eukaryotic systems (i.e., mouse brain and *Paramecium caudatum* (33)). This technique relies however on thin biological sections, which are embedded into an optimized matrix. Because of this extensive sample preparation and the relatively long measurement times, MALDI-MSI is slow in throughput. Additionally, freeze-thaw cycles as required for sectioning and subsequent embedding can cause LD mobilization and flow in the tissue. Magnetic resonance imaging is well suited to visualize oil bodies in vivo from plants to humans (34,35). With a resolution of around 10 $\mu$m in $x$- and $y$-directions and 100 $\mu$m in the $z$-direction, as well as the capability to image centimeter scale samples, this technique is applicable to investigate the structure of TAGs in larger lipid depots in entire organisms (36), but it is not readily equipped to spatio-chemically resolve fine structures (i.e., individual LDs). Vibrational spectroscopy (e.g., spontaneous Raman and CRS) uses intrinsic molecular vibrations to visualize different macromolecular species, such as all lipids, all DNA (or RNA), or all proteins, and can be used both in vitro and in vivo (30,37). CARS microscopy, which is one type of CRS, relies on a resonant enhancement via nonlinear excitation to achieve higher signal strengths compared to spontaneous Raman scattering (for highly concentrated species), and the blue-shifted signal light is readily separated from linear fluorescence background. Using a hyperspectral approach, chemical information can be mapped with submicrometer resolution with complete vibrational spectra at each spatial location (38). From these spectra, ratiometric quantities have been employed to map TAG saturation in mammalian cells (39,40) and algae (41). However, these analyses are not equipped to study TAG chain length in combination with saturation. For that purpose, a least-squares decomposition of single-point Raman spectra from intracellular droplets has been employed by Schie et al. (42) to track the uptake of oleic and palmitic acid. Similarly, a factorization approach of hyperspectral CARS data has been used to study lipid dynamics in human stem cells (43). The latter two approaches focus on quantifying the amount of a small subset of known fatty acids that were supplied to the culture medium and ultimately incorporated in the LDs; however, the data were not analyzed in a way that permitted determining the chain length and saturation of TAGs in native (unstimulated), single LDs.

In this work, we employ broadband hyperspectral CARS (BCARS) microscopy combined with a least-squares decomposition to map the average number of C=C double bonds and chain length in TAGs in native LDs with submicrometer spatial resolution and ~5–100 ms acquisition times. We demonstrate the applicability of this approach in artificial emulsions, microalgae, yeast, and mammalian cells for which our results compare favorably with mass spectrometry results. This analytical methodology should be readily transferable to other experimental setups and provides meaningful numbers that can be understood in a physiological context.

## MATERIALS AND METHODS

### Materials

TAG and oil standards as well as bovine serum albumin (BSA) were purchased from Sigma-Aldrich (Darmstadt, Germany): glyceryl trioctanoate (8:0, T9126, CAS 538-23-8), glyceryl tripalmitate (16:0, T5888, CAS 555-44-2), glyceryl tripalmitoleate (16:1, T2630, CAS 20246-55-3), glyceryl tristearate (18:0, T5016, CAS 555-43-1), glyceryl trioleate (18:1, T7140, CAS 122-32-7), glyceryl trilinoleate (18:2, T9517, CAS 537-40-6), glyceryl trilinolenate (18:3, T6513, CAS 14465-68-0), canola oil (46961, CAS 12096-03-0), cottonseed oil (47113, CAS 8001-29-4), olive oil (47118, CAS 8001-25-0), peanut oil (47119, CAS 8002-03-7), soybean oil (47122, CAS 8001-22-7), sunflower seed oil (47123, CAS 8001-21-6), and BSA (05470, CAS 9048-46-8). Long-chained TAGs were purchased from Larodan (Solna, Sweden): glyceryl triarachidonoyl (20:4, 33-2040,

CAS 23314-57-0) and glyceryl tridocosahexaenoyl (22:6, 33-2260, CAS 124596-98-1).

## Pure and diluted oils

Pure oils were measured either at room temperature (8:0, 16:1, 18:1, 18:2, 18:3, 20:4, 22:6) or at 86°C (16:0, 18:0) with a homebuilt Peltier temperature stage. Oils diluted in $CCl_4$ and toluene-d8 were measured at 10°C.

## Stabilized emulsions

Oils were encapsulated at 10 vol % in 3 wt % agarose with low gelling temperature after thorough vortexing and were sandwiched between two glass coverslips (#1). Fig. S1, *A* and *B* shows that heterogeneous sized LDs are formed this way. Because of the vortexing, water-oil-water double emulsions can form (Fig. S1 *B*, *droplets with dark spots*). They were excluded from this study.

## Cell culture

3T3-L1 adipocytes were cultured on glass-bottom Petri dishes and differentiated as previously described (44,45). RAW 246.7 and HEK-293 cells were cultured on glass and grown in medium supplemented with 2 mg $mL^{-1}$ low-density lipoprotein for 24 and 48 h, respectively. Before imaging, all cells were fixed in 4 vol % paraformaldehyde. CENPK 113-11C *Saccharomyces cerevisiae* and *Yarrowia lipolytica*, TAG-producing yeast strains, were cultured as previously described (8,46) and fixed in paraformaldehyde. *Nannochloropsis* species (sp.; CCAP211/78) was cultivated according to the methods used for strain maintenance and flask cultivation detailed in Mayers et al. (47). Cultures were allowed to deplete media nitrogen for the purposes of this analysis to generate cells with higher lipid content. Both yeast and algae cells were subsequently encapsulated in 3 wt % agarose with low gelling temperature and sandwiched between two coverslips. An overview of all used samples can be found in Fig. S1, *C*–L showing the morphology of the different cell types as well as their intracellular LDs.

## CARS microscopy

LDs in artificial emulsions, 3T3-L1 adipocytes, yeast, and algae were visualized with CARS microscopy. A specific molecular vibration (i.e., the symmetric $CH_2$ stretching at 2845 $cm^{-1}$) is targeted with the fields generated by two laser pulses (with energies $\omega_{pump}$ and $\omega_{Stokes}$) overlapped in time and space. A third pulse ($\omega_{probe}$) is then used to generate the CARS signal ($\omega_{anti\text{-}Stokes} = \omega_{pump} + \omega_{Stokes} - \omega_{probe}$). The CARS imaging was performed with an SP 5 II TCS CARS microscope (Leica, Mannheim, Germany) equipped with a picosecond pulsed laser source at 817 and 1064 nm (Angewandte Physik & Elektronik, Berlin, Germany) using a water immersion objective (L 25×, NA = 0.95; Leica) to achieve tight focusing conditions. CARS signals were collected in the forward direction with a Leica CARS 2000 filter set in front of the photomultiplier tube. For 3T3-L1 adipocytes, autofluorescence was collected in the epi-direction using the Leica fluorescein isothiocyanate filter set.

## BCARS microscopy

The homebuilt setup with custom software written in LabVIEW (National Instruments, Austin, TX) has been described in detail previously (48). Briefly, from a dual-output laser source (subnanosecond pulses, 32 kHz, Leukos-CARS; Leukos, Limoges, France), a supercontinuum Stokes beam is generated using a photonic crystal fiber (100 $\mu W$ $nm^{-1}$; 1050–1600 nm). This Stokes beam was then overlapped with the fundamental pump (and probe) beam at 1064 nm in the focus of an inverted microscope (Eclipse Ti; Nikon, Minato, Japan) equipped with an XYZ Piezo Stage (Nano-PDQ 375 HS; Mad City Labs, Madison, WI) for sample scanning. A near-infrared objective (100×, NA 0.85; PE IR Plan Apo; Olympus, Tokyo, Japan) was used to tightly focus the two beams onto the sample, with the resulting CARS signals being collected in the forward direction by a 10× objective (M-10×, NA 0.25; Newport, Irvine, CA) for all samples except the mammalian cells for which a water dipping collection (W N-Achroplan 10×, NA 0.3; Zeiss, Oberkochen, Germany) was employed for collection. The collected CARS signal was filtered through a notch (NP03-532/1064-25; Semrock, Rochester, NY) and short-pass (FES1000; Thorlabs, Newton, NJ) filter before being dispersed in a spectrometer (300 lines $mm^{-1}$; 1000 nm blaze; Shamrock 303i; Andor, Belfast, Northern Ireland) and detected on a deep-depletion CCD (Newton DU920P-BR-DD, Andor) with a spectral pitch of 4 $cm^{-1}$ $pixel^{-1}$. Images were collected with 0.1–0.5 $\mu$m step sizes in the *xy*-plane and each pixel was illuminated for 5–100 ms (Table S1).

## Hyperspectral data analysis

All data were analyzed with custom routines in IgorPro (version 6.37; WaveMetrics, Portland, OR) and MATLAB (R2016a; The MathWorks, Natick, MA). First, the imaginary component of the third-order Raman susceptibility was retrieved with a modified Kramers-Kronig algorithm (49) with glass as reference followed by error phase correction using either 1) an iterative noise-maintaining approach (50), which is model free with the use of a second-order Savitzky-Golay smoothing filter over 101 spectral points (404 $cm^{-1}$) for mixed samples or 2) an iterative fourth-order polynomic function for pure samples (50). The resulting spectra are referred to as Raman-like (RL) in accordance with previous publications (38,51). The spectral points between 1200–1786 $cm^{-1}$ and 2828–3102 $cm^{-1}$ were selected for all subsequent processing and fitting.

## Maps for lipid chain length and number of C=C bonds

The fitting method was further developed from Waschatko et al. (52) and applied to full hyperspectral images. All RL spectra were aligned and normalized such that the maximal value of the 1440 $cm^{-1}$ $CH_2$ deformation peak was one. A training matrix was formed from the RL spectra of 8:0 TAG, 16:1 TAG, 18:1 TAG, 18:2 TAG, 18:3 TAG, 20:4 TAG, and a mixture of 50% 8:0 and 50% 18:1 (v/v) (Fig. S2, *spectra*) and 100 mg $mL^{-1}$ BSA in MilliQ-water (Millipore, Burlington, MA). A least-squares decomposition with known covariance (Fig. 1 *A*; Table 1) was used to generate three components representing the presence of TAGs ($C_{TAG}$), the number of C=C bonds per chain ($C_{\#C=C}$), and the number of $CH_2$ per chain ($C_{\#CH2}$). The spectrum of 100 mg $mL^{-1}$ BSA was used as a generic protein component ($C_{protein}$). Further, a fifth component ($C_{dilution}$) attributed to spectral changes upon dilution of TAGs was generated using a global fitting on spectra of diluted 16:1 and 18:1 TAG in $CCl_4$ (Fig. S3). Therefore, four components were assumed: pure 16:1 TAG, pure 18:1 TAG, pure $CCl_4$, and an unknown dilution component. This dilution component was then refined in a global fitting approach to best fit the seven diluted spectra.

The component spectra, as well as all spectra to be fitted, were then interpolated in the wavenumber dimension by a factor of six to ensure subpixel shifts were possible before fitting to a target spectrum with Eq. 1.

$$\begin{aligned} Meas(g) = {} & a \times C_{TAG}(f - f_0) + b \times C_{\#C=C}(f - f_0) \\ & + c \times C_{\#CH2}(f - f_0) + d \times C_{protein}(f - f_1) \\ & + e \times C_{dilution}(f - f_2) + m \times f + n, \end{aligned} \tag{1}$$

where *a, b, c, d,* and *e* are weights of the five components, *f* is the Raman shift, and $f_0$, $f_1$, and $f_2$ allow for slight shifts of lipid, protein, and dilution

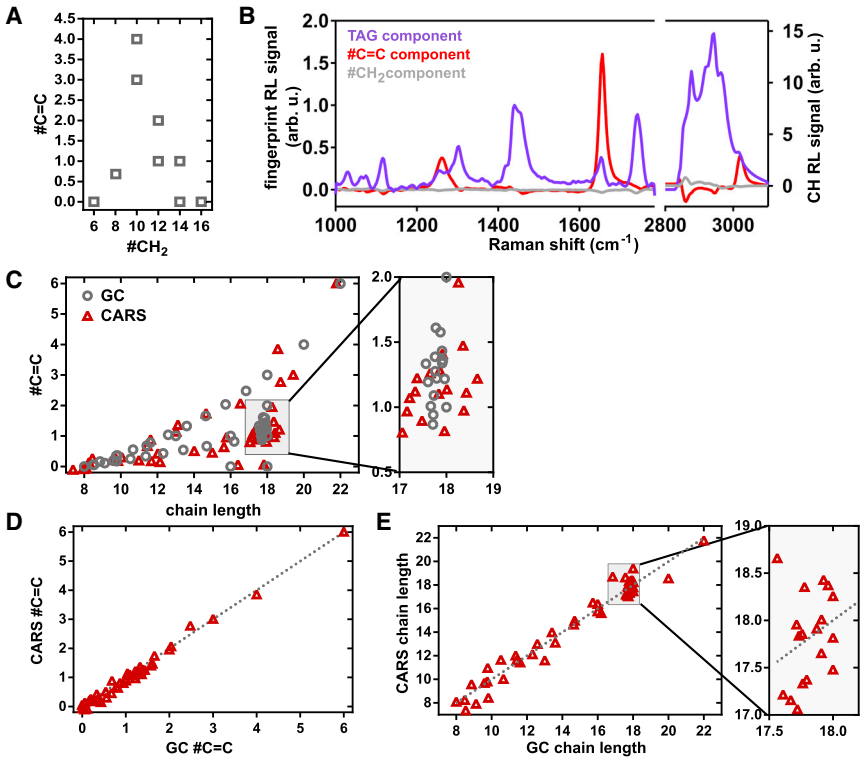


FIGURE 1 #C=C bonds and number of $CH_2$ ($\#CH_2$) groups for TAGs used in the training matrix to retrieve TAG, #C=C, and $\#CH_2$ components (*A*). The covariance table (Table 1) and spectra in (*A*) were used to produce three lipid components, which were used to recalculate experimental spectra. (*B*) A set of standard food oils, their mixtures, and TAG mixtures were analyzed and compared to the same quantities extracted from GC-MS measurements (*C–E*). The closer the red triangles (BCARS) are to the gray dots/line (GC-MS), the smaller the error. In (*D*) and (*E*), dotted lines represent perfect agreement for the BCARS and GC-MS methods. To see this figure in color, go online.

components in the measured data (*Meas*). The values for $f_0$, $f_1$, and $f_2$ were always found to be less than 4 $cm^{-1}$ and thus less than the frequency spacing between adjacent CCD pixels (hence the necessity for interpolation); this is reasonable given the months' timespan over which the data reported here was acquired. $m$ and $n$ allow for linear baseline offsets to be accounted for. For the spectral fitting of pure TAGs, oils, and their mixtures, only the three lipid components were used; for emulsions, the dilution component was added; for cells, the protein and dilution components were added (all seed values are in Table S2). All weights for the components were constrained to be $> -0.1$.

To recalculate the number of double bonds per chain and the average chain length of the TAG from the fit parameters, the weight of all components were divided by $a$ to normalize $a$ to one, as was done in the training matrix. This allowed a readout of the #C=C as $b/a$, $\#CH_2$ as $c/a$, and the chain length as $2\times(\#C{=}C) + (\#CH_2) + 2$ (accounting for end groups). For image analysis, a mask was generated based on the $CH_2$ (2845 $cm^{-1}$) intensity of the RL spectra to include only lipid spectra in the fitting, then a pixel-by-pixel fitting was done based on the method described above for single spectra. After the image fit, an additional threshold ensuring chain lengths were within 12–24 and $\#C{=}C > -0.1$ was applied to all images to eliminate unreasonable values typically found at droplet borders where the fitting failed because of lipid peak intensities falling below the level necessary for accurate fitting (Fig. S4).

**TABLE 1 Known Covariance for Least-Squares Decomposition**

| Molecule | TAG Component | #C=C (per Chain) Component | $\#CH_2$ (per Chain) Component |
|---|---|---|---|
| 8:0 TAG | 1 | 0 | 6 |
| 16:0 TAG | 1 | 0 | 14 |
| 16:1 TAG | 1 | 1 | 12 |
| 18:0 TAG | 1 | 0 | 16 |
| 18:1 TAG | 1 | 1 | 14 |
| 18:2 TAG | 1 | 2 | 12 |
| 18:3 TAG | 1 | 3 | 10 |
| 20:4 TAG | 1 | 4 | 10 |
| 50% 8:0 and 50% 18:1 (v/v) | 1 | 0.68 | 8.05 |

## Statistical testing

Errors of our method with respect to the gas chromatography values are expressed as root mean-square (RMS) error. The data for diameter, TAG chain length, and TAG saturation in the two adipocyte LD populations were tested for normality with a D'Agostino-Pearson omnibus normality test using GraphPad Prism 6.0. All data were considered normally distributed, and an unpaired two-tailed *t*-test with Welch's correction was employed to analyze statistical significance between LDs of different sizes. *p*-values were ranked as follows: $p > 0.05$ (not significant), $p \leq 0.05$, $p \leq 0.01$, $p \leq 0.001$, and $p \leq 0.0001$.

## RESULTS

### BCARS decomposition characterizes standard oils and TAG mixtures with ± 0.69 chain length and ± 0.15 #C=C accuracy

To establish a method for extracting average chain length and number of C=C bonds from images of TAGs, we first produced a least-squares decomposition with known covariances using a training matrix of TAGs. Our training matrix consisted of quantitative, linear RL spectra from BCARS spectra (see Materials and Methods) of TAGs and their mixtures spanning the physiological range of fatty acid double

bonds and chain lengths (Fig. 1 *A*; Table 1, full spectra in Fig. S2). From the training matrix, three components could be extracted (Fig. 1 *B*): a TAG glycerol backbone component, the number of C=C bonds per TAG, and the number of $CH_2$ groups in the TAG chain. The TAG component represents the most common spectral features found in all TAGs in the training matrix, whereas the number of C=C and $CH_2$ components represent spectral changes that depend on the number of C=C double bonds or the chain length, respectively, as reflected in the known covariances (Table 1).

Because our BCARS has a focal volume of 0.5 × 0.5 × 3.5 $\mu m^3$ (49,51), this method produces a molar average chain length and number of C=C bonds for all TAGs within this volume. The chain length discussed here refers to the average number of carbons in one TAG chain, including the ester and $CH_3$ end groups. Using the three lipid components, the number of C=C bonds, and the chain length from standard oils, mixtures of standard oils and TAG mixtures were derived (Table S3). The resulting parameters derived from the BCARS method were compared to the molar averages from GC-MS measurements to evaluate the RMS error in our method. The overall agreement between the BCARS and GC-MS measurements, especially when both chain length and #C=C are considered, is clear (Fig. 1 *C*). On average, our method is accurate for the number of C=C to within ±0.15 (Fig. 1 *D*) and for the chain length to within ±0.69 $CH_2$ (Fig. 1 *E*). The CARS values evenly vary around the GC-MS values, suggesting no systematic over- or underestimation.

## Imaging chain length and #C=C in emulsified oil droplets

Having established the ability to accurately quantify TAG chemistry in individual spectra, we next tested the ability to map TAG chemistry in space. For that purpose, we acquired images of olive oil droplets in oil-in-water emulsions to determine the accuracy of our method in a heterogeneous sample. Olive oil was mixed with melted agarose and vortexed. This sample preparation method generated oil-in-water emulsions but also more complex water-in-oil-in-water double emulsions (Fig. S1 *B*). Thus, we expected more complex spectra and the emulsions indeed showed a different spectral shape compared to pure oils (Fig. 2 *A*), similar to what we found in oil diluted in organic solvents. To account for this shape of the emulsified oil, we recorded spectra from a set of oils (18:1 and 16:1 TAGs) diluted in carbon tetrachloride (Fig. S3) and used a global fitting approach to generate a spectral component that captured the spectral changes caused by dilution (Fig. 2 *B*). We validated this component against other diluted oils (Table S4), which confirms the validity of the approach. The inclusion of this component allows us to fit spectra from the olive oil emulsions and obtain the #C=C and chain length values within our RMS error from pure oils (Fig. 2, *C* and *D*) even if there are small-scale impurities that effectively dilute the oil. With a focal volume of 0.5 × 0.5 × 3.5 $\mu m^3$, we expect a larger fitting error for smaller droplets because of the increased proportion of matrix (and corresponding decreasing proportion of lipid) in the spectra.

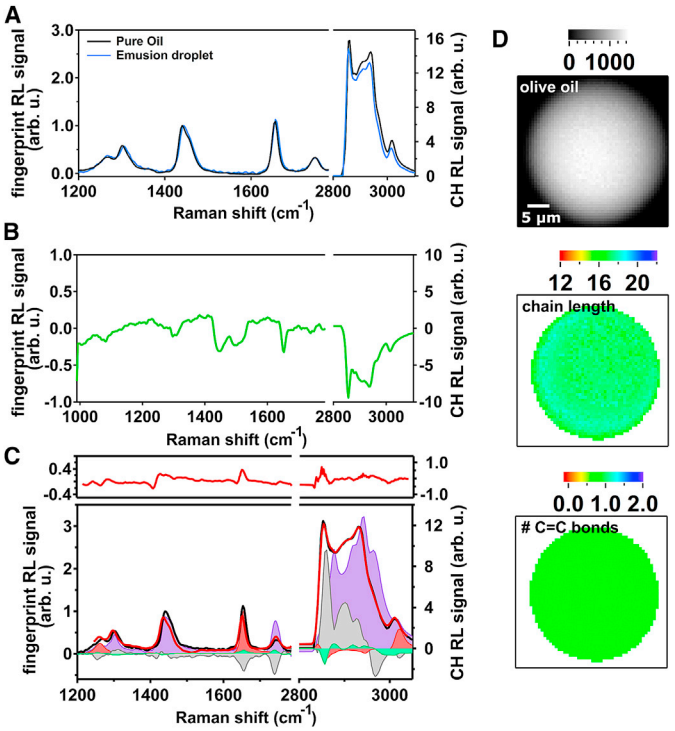


FIGURE 2 Normalized (to the intensity at 1440 $cm^{-1}$) spectra of pure olive oil (*black*) and olive oil in the stabilized emulsion (*blue*) (*A*). Note the different ordinate axes for the fingerprint (1200–2000 $cm^{-1}$, *left*) and CH stretch (2800–3100 $cm^{-1}$, *right*) regions. Derived component representing the spectral differences caused by dilution of oils (*B*). Reconstruction (*red line*) of the experimental spectrum from the middle of the droplet (*black line*, normalized to 1440 $cm^{-1}$) using the TAG (*violet fill*), #C=C (*red fill*), #CH2 (*grey fill*), and dilution (*green fill*) components (*C*). Fitting residuals are plotted as red line in the upper panel in (*C*). Image of an olive oil emulsion droplet and computed maps for chain length and #C=C bonds (*D*) using the components from (*C*). Comparing chain length and #C=C values for small ($n$ = 67) and big ($n$ = 12) droplets, a tendency to read out longer chains can be found for the smallest droplets (*E*). There is no significant difference in the number of double bonds depending on droplet size. Values are displayed as mean ± SD. Significance was determined using an unpaired *t*-test with Welch's correction, and *p*-values are classed as not significant is >0.05 and ** < 0.01. To see this figure in color, go online.

For this purpose, we investigated the average chain length and number of double bonds depending on droplet diameter in the same olive oil sample (Fig. 2 *E*). For smaller droplets (below 2 $\mu$m), we found a significant likelihood to detect longer chains in droplets but no difference in our ability to retrieve the average number of double bonds assuming that the droplet composition does not vary with differing size. By adding random (Gaussian) noise with increasing SD to the spectrum of olive oil, we found that decreasing spectral quality (signal/noise) increases the scatter in values predicted by our fitting method as expected (Fig. S5).

## Determining LD TAG chemistry in situ in biological organisms

The biological samples we studied had a broad range of LD sizes. *S. cerevisiae* and *N.* sp. both have submicron-sized LDs (Fig. S1). This LD size is small compared to their cellular volume, different from mammalian adipocytes, which can exhibit LDs that are several tens of microns in diameter and occupy the entire intracellular space. These submicron-sized lipid volumes can be challenging to analyze using standard methods like lipid extraction followed by GC-MS for which large culture volumes can be required, and cell sizes can approach the limit of mass spectrometry imaging. We also included *Y. lipolytica*, a yeast specialized in the production of lipids as an alternative microorganism with larger LDs. For these microorganisms, LDs have been identified label free with single-frequency CARS microscopy of the symmetric $CH_2$ vibration (at a frequency of 2845 $cm^{-1}$) (53,54). As mammalian examples, differentiated 3T3-L1 adipocytes, low density lipoprotein (LDL)-fed RAW, and LDL-fed HEK cells were investigated. As stated above, differentiated 3T3-L1 cells have LDs that can occupy nearly the entire cell (of order 10 $\mu$m), whereas LDL-fed RAW and HEK cells exhibit smaller, micron-sized LDs (Fig. S1).

For these complex biological samples, a fifth component (i.e., the spectrum of BSA) was included to be able to account for a generic protein signal (Fig. 3 *A*), which will certainly be found in close proximity to LDs in these samples. This proximity will lead to spectra containing a mixture of protein and lipids at the LD edges at the very least and possibly even spectra in the center of the LD for droplets that are smaller than the axial span of our excitation volume. Hyperspectral data sets from the different biological species were fit with all five components as described in the Materials and Methods, and we produced images of carbon chain length and the number of C=C bonds (Fig. 3 *D*) from them. Immediately obvious from the images in Fig. 3 *D* is that the LDs in all biological systems are considerably more heterogeneous than in the stabilized emulsions, as expected. When averaging over all images for each type of sample (aggregating from the single-pixel basis), we found the average chain length in LDs spans from 16.7 to 18.8 over all species (Fig. 3 *B*), whereas more variety (compared to the average chain length over all species) was found in the average number of double bonds, which spans from 0.29 to 0.94 (Fig. 3 *C*).

The results from BCARS imaging of lipid chemistry for *Y. lipolytica*, representative of microorganisms, and 3T3-L1, representative of mammalian cells, were quantitatively compared to the GC-MS data from extracted neutral lipids (Supporting Materials and Methods, Method S1; Table S5). For *Y. lipolytica* and 3T3-L1 GC-MS, we found an average chain length/#C=C of 17.6/0.28 and 16.1/0.25, respectively, which was within our experimental error from the spatial averages shown in Fig. 3, *C* and *D*.

Although all samples showed spatial variation, we were particularly drawn to that seen in the differentiated 3T3-L1 cells because there seemed to be two major classes of LDs in cells: 1) larger LDs that were fewer in number and 2) smaller LDs that were quite numerous. Further, from looking at the images in Fig. 3 *D*, these LD classes seemed to contain different TAGs. Indeed, we found a weak inverse correlation between the droplet diameter number of double bonds (Fig. 4 *A*). If the droplets are split into two approximately equal groups according to their diameter, the difference becomes significant (Fig. 4 *B*). Small LDs ($<2$ $\mu$m) have an average of 0.35 double bonds per chain, whereas big LDs have an average of 0.31 double bonds per chain.

## DISCUSSION

Lipid depots are present in many species and their neutral lipid composition can be linked to certain diseases or is a potential engineering target for bioenergy production. The majority of studies to date focused on the changes in LD TAG composition have been based on data collected from large cell populations and thus only few insights into LD chemical heterogeneity have been made (55). In this study, we present a method to extract quantitative information about spatial heterogeneity in LD chemistry in terms of TAG chain length and number of double bonds with submicrometer resolution from noninvasive, BCARS imaging. Although mass spectrometry can deliver complete chemical identification and micron-scale spatial resolution, it relies on extensive sample preparation, such as lipid extraction (and chromatography) or embedding in complex matrix. Moreover, large and clean samples are required, which are not always available. Using a noninvasive optical method allows analysis of individual LDs in single cells as well as standard oils within minutes. Another feature of the BCARS method shown here is the $\sim$2-fold better spatial resolution (48) compared to state-of-the-art imaging mass spectrometry ($\sim$1.4 $\mu$m resolution (33)). Principally, the resolution of our method is limited by diffraction to $\sim$500 nm with our current objective; however, better-quality objectives having a higher NA and better chromatic performance would allow characterization of even smaller LDs than shown here. Finally, in contrast to previous

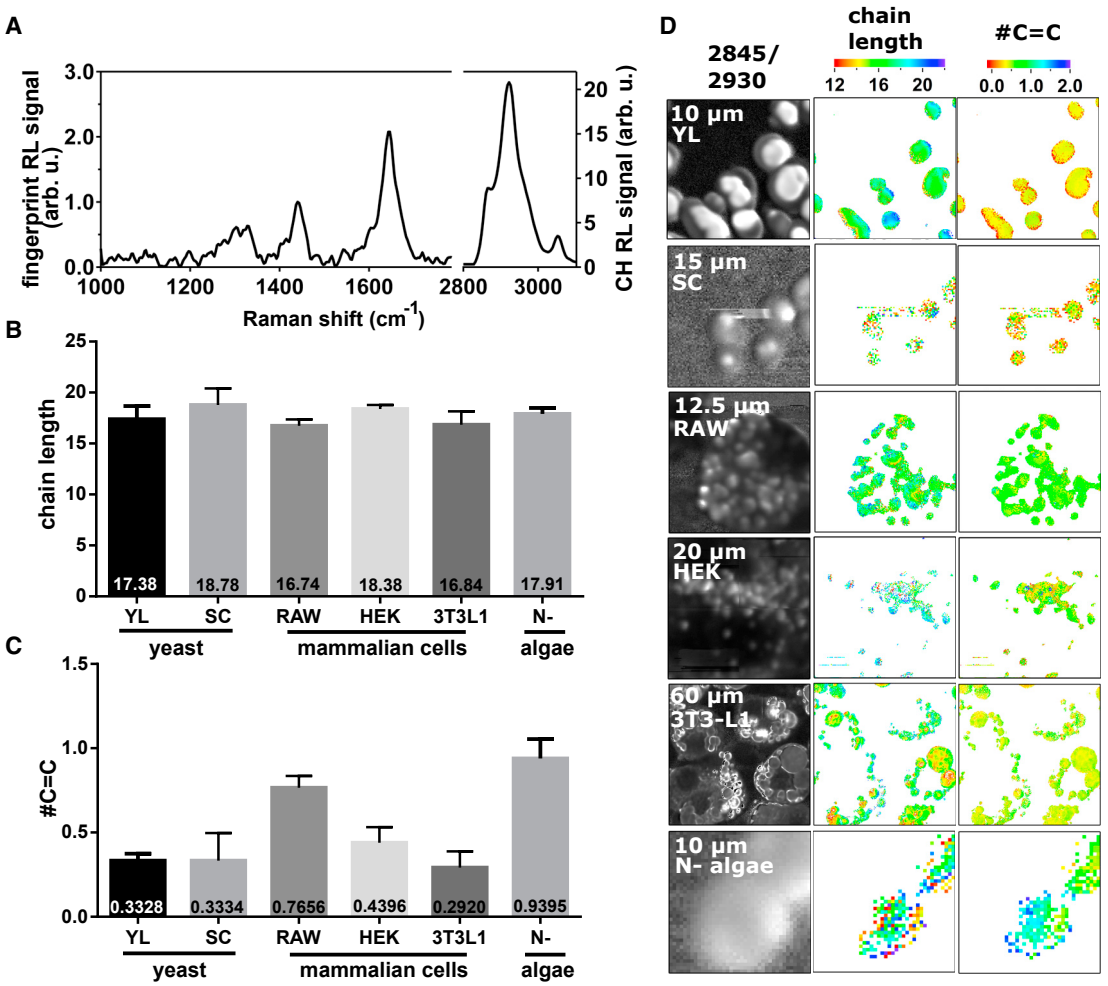


FIGURE 3 A generic protein component (BSA) was added as a fifth component to improve the fitting of LD spectra from complex biological samples for which several macromolecule classes can be inside the focal volume (*A*). BCARS images from different biological species were analyzed, and the average chain length (*B*) and the number of double bonds (*C*) were determined by averaging all lipid containing pixels from multiple different cells in each category. Representative images displaying the cellular morphology (via the ratio of 2845 $cm^{-1}$ over 2930 $cm^{-1}$) highlighting intracellular lipid droplets (LDs) and the plasma membrane, chain length, and #C=C distribution are shown in (*D*). All chain length and #C=C images are color coded in the same way as shown in the top panel. Contrast from the 2845 $cm^{-1}$ vibration alone is shown in Fig. S6. The number of analyzed images is *Y. lipolytica* (YL) $n = 5$, *S. cerevisiae* (SC) $n = 5$, RAW $n = 4$, HEK $n = 3$, 3T3-L1 $n = 27$, and nitrogen starved *N. sp.* (N-) $n = 5$. Values are displayed as mean ± SD. To see this figure in color, go online.

studies employing spectral CARS (39,40), our method does not return ratiometric quantities of TAGs but rather physiologically descriptive numbers for TAG chemistry that are directly comparable to other techniques. We note that it has been previously shown that CARS microscopy could be used to extract vol/vol concentration of certain lipids in lipid-fed cells as compared to cells with no exogenous lipid feeding (43). The method shown here provides a similar capability while allowing direct lipid quantification of arbitrary TAG chemistry in unstimulated cells as well.

## Method reliability

Standard TAGs were used to establish the training matrix needed to generate the lipid components for the known covariance least-square fitting, and food oils were subsequently used for the estimation of the standard error against industry-standard GC-MS. The error in our method is highest for lower chain lengths and higher degrees of saturation, that is, a lower number of C=C. Physiologically relevant TAGs with chain lengths from 16 to 18 C and 1–2 C=C bonds can be determined with high accuracy. Specifically, for chains lengths below 16, the RMS deviation relative to the average chain length is ~6.4%, whereas for chain lengths above 16, the RMS deviation is 3.7%. For oils with 0–1 double bonds on average, the relative deviation is 33.1%, whereas the metric is 10.6% for >1 C=C bond. The error is evenly distributed around the GC-MS values, suggesting that there is no systematic error, for example, by an insufficient training matrix, causing these errors.

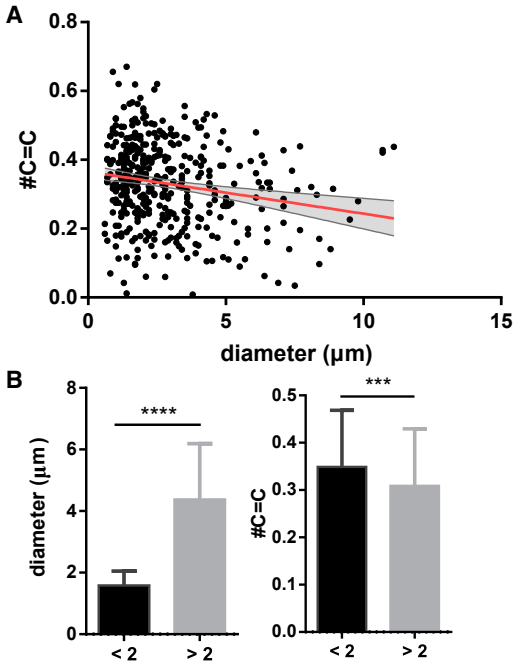


FIGURE 4 The number of double bonds shows a negative correlation with droplet diameter (*A*). Splitting the droplets into two groups with a diameter below ($n = 236$) or above ($n = 195$) 2 $\mu$m, we find that the chemical differences for the LD groups are statistically significant (*B*). Values are displayed as mean ± SD. Significance was determined using an unpaired *t*-test with Welch's correction, and *p*-values are classed as *** $< 0.001$ and **** $< 0.0001$. To see this figure in color, go online.

Instead, the deviation can be viewed as the true error of the method and in repeatability of the acquired data, which were taken over 2 years on a multiuser BCARS microscope. As the concentration of TAG in LDs reduces and the TAG-based spectral features become hidden by noise, the method reliability decreases, as expected for a multiparameter fitting algorithm.

## In situ lipid mapping

When applying our method to more complex systems, like cells, other aspects must be considered for the spectral decomposition. If the cell had an LD size approaching or below our focal volume, as was the case for algae and yeast cells, it was necessary to include a protein and dilution component in the fitting because individual pixels in the lipid-rich regions will undoubtedly contain mixed cytosol and lipid signals in the spectral response. Yeast and algae with LDs $< 0.5$ $\mu$m are clear examples for which the technique meets its limitations because no individual LDs can be seen with the BCARS spectral imaging. Corroborating this finding, we found that the determination of chain lengths becomes slightly skewed for smaller LDs $< 2$ $\mu$m with a higher probability to detect longer chains. This results from an increased contribution from the surrounding matrix and a reduced signal/noise of TAG-specific peaks. Nevertheless, we propose that one could use our method to compare lipid biochemistry among individual cells, even for small LDs, as a way to compare different biological conditions for the same cell type. In such experiments, it would be important to simultaneously record droplet size and compare LDs with similar sizes.

Although LDs in microalgae are to date not well understood (56), it has been found that the cellular lipid storages in *Nannochloropsis* increase in size and number under nitrogen depletion (57). It has also been shown that the same strain of microalgae grown under nitrogen starvation contains around 15.0 ± 1.3% saturated fatty acids and 21.2 ± 1.7% unsaturated fatty acids (47). This results in an average chain length of 16.9 with 1.4 double bonds. The batch we analyzed similarly shows high unsaturation (0.94 C=C).

For *yarrowia lipolytica*, where each cell has a >500 nm TAG-filled LD and differentiated 3T3-L1, a model for mammalian adipocytes, we found good agreement among BCARS imaging, GC-MS measurements, and existing literature (58). However, the GC-MS method required extensive sample preparation, such as TAG extraction from millions of cells (Supporting Materials and Methods, Method S1), whereas the BCARS method can be applied on as few as 5–10 cells. Including the time for image acquisition and image fitting (on a standard desktop PC), results can be obtained within 5 h. Interestingly, when looking within single LDs, the adipocytes show the saturated TAGs located on the outer parts of the droplet, almost the exact opposite for what was seen in algae (and yeast). When comparing among LDs within adipocytes, we found that the unsaturation of TAGs inversely correlates with the size of the LDs, with large LDs having an 11% lower number of C=C bonds than small LDs on average. During differentiation from mesenchymal precursors into adipocytes, LD sizes typically increase, whereas the LD number per cell decreases. It has previously been suggested that the size of the LDs in 3T3-L1s reflect the "age" of the droplet in that a small droplet is recently formed and that large droplets are older (59). Combined with the fact that lipid profiles of 3T3-L1s change during differentiation, with longer chains and more unsaturated fatty acids diminishing during the differentiation (60), this supports our finding that large (old) LDs are less unsaturated compared to small (young) LDs.

## CONCLUSION

In this work, we present a method to generate a fast overview of average lipid species, in situ, in mammalian and nonmammalian cells with up to 500 nm spatial resolution. This methodology allows for a somewhat detailed understanding of intra-LD, inter-LD, and cell-to-cell TAG chemical variation with virtually no sample preparation. Physiologically meaningful and comparable lipid quantification is achieved, which shows high accordance with

GC-MS-derived TAG chain length and saturation for pure oils and cellular samples. Because of the fast image acquisition and noninvasive nature of our method, future applications to study dynamic lipid biochemistry in cells, tissues, or in food emulsions will be enabled with much improved accuracy because of the straightforward in situ measurement conditions.

## SUPPORTING MATERIAL

Supporting Material can be found online at https://doi.org/10.1016/j.bpj.2019.04.036.

## AUTHOR CONTRIBUTIONS

A.P. and S.H.P conceived the idea, designed the project, and wrote the majority of the manuscript. A.P. collected the majority of data and analyzed all data, Y.W. contributed spectra of diluted oils, and S.K. and C.B. contributed to the cell culture. C.B. and M.B. commented and edited the text. All authors read and approved the final version of the text.

## ACKNOWLEDGMENTS

The authors thank Charlotta Olofsson, Gothenburg University, for the provision of 3T3-L1 cells; David Bergenholm and Jens Nielsen, Chalmers, for *S. cerevisiae*; Oliver Konzock, Chalmers, for *Y. lipolytica*; Joshua J. Mayers, Chalmers, for *N.* sp.; Mischa D. Schwendy, Max Planck Institute for Polymer Research (MPIP), for RAW and HEK cells; Frederik F. Fleissner and Marc-Jan van Zadel, MPIP, for support with the BCARS setup; Xiao Ling, MPIP, for input to the global fitting; and Pernilla Wittung-Stafshede, Chalmers, for great scientific discussions.

The research leading to these results received funding from the European Union's Seventh Framework Programme (FP7/2007-2013) under grant agreement n°607842. Additional funding was received from Kungliga Vetenskaps- och Vitterhets-Samhället, Wilhelm och Martina Lundgrens Stiftelse, Marie Curie Foundation (CIG322284), and the Human Frontiers in Science Program (RGP0045/2018).

## REFERENCES

1. Thiam, A. R., R. V. Farese, Jr., and T. C. Walther. 2013. The biophysics and cell biology of lipid droplets. *Nat. Rev. Mol. Cell Biol.* 14:775–786.
2. Thiam, A. R., and M. Beller. 2017. The why, when and how of lipid droplet diversity. *J. Cell Sci.* 130:315–324.
3. Murphy, D. J. 2001. The biogenesis and functions of lipid bodies in animals, plants and microorganisms. *Prog. Lipid Res.* 40:325–438.
4. Goodpaster, B. H., J. He, …, D. E. Kelley. 2001. Skeletal muscle lipid content and insulin resistance: evidence for a paradox in endurance-trained athletes. *J. Clin. Endocrinol. Metab.* 86:5755–5761.
5. Lee, Y., H. Hirose, …, R. H. Unger. 1994. Beta-cell lipotoxicity in the pathogenesis of non-insulin-dependent diabetes mellitus of obese rats: impairment in adipocyte-beta-cell relationships. *Proc. Natl. Acad. Sci. USA.* 91:10878–10882.
6. Shimabukuro, M., M. Higa, …, R. H. Unger. 1998. Lipoapoptosis in beta-cells of obese prediabetic fa/fa rats. Role of serine palmitoyltransferase overexpression. *J. Biol. Chem.* 273:32487–32490.
7. Listenberger, L. L., X. Han, …, J. E. Schaffer. 2003. Triglyceride accumulation protects against fatty acid-induced lipotoxicity. *Proc. Natl. Acad. Sci. USA.* 100:3077–3082.
8. Wei, Y., M. Gossing, …, J. Nielsen. 2017. Increasing cocoa butter-like lipid production of Saccharomyces cerevisiae by expression of selected cocoa genes. *AMB Express.* 7:34.
9. van der Schoot, C., L. K. Paul, …, P. L. Rinne. 2011. Plant lipid bodies and cell-cell signaling: a new role for an old organelle? *Plant Signal. Behav.* 6:1732–1738.
10. Beller, M., D. Riedel, …, R. P. Kühnlein. 2006. Characterization of the Drosophila lipid droplet subproteome. *Mol. Cell. Proteomics.* 5:1082–1094.
11. Martin, S., and R. G. Parton. 2005. Caveolin, cholesterol, and lipid bodies. *Semin. Cell Dev. Biol.* 16:163–174.
12. Wilfling, F., H. Wang, …, T. C. Walther. 2013. Triacylglycerol synthesis enzymes mediate lipid droplet growth by relocalizing from the ER to lipid droplets. *Dev. Cell.* 24:384–399.
13. Cushman, S. W., and M. A. Rizack. 1970. Structure-function relationships in the adipose cell. 3. Effects of bovine serum albumin on the metabolism of glucose and the release of nonesterified fatty acids and glycerol by the isolated adipose cell. *J. Cell Biol.* 46:354–361.
14. Gluchowski, N. L., M. Becuwe, …, R. V. Farese, Jr. 2017. Lipid droplets and liver disease: from basic biology to clinical implications. *Nat. Rev. Gastroenterol. Hepatol.* 14:343–355.
15. Bosma, M. 2016. Lipid droplet dynamics in skeletal muscle. *Exp. Cell Res.* 340:180–186.
16. Liu, P., Y. Ying, …, R. G. Anderson. 2004. Chinese hamster ovary K2 cell lipid droplets appear to be metabolic organelles involved in membrane traffic. *J. Biol. Chem.* 279:3787–3792.
17. Butterworth, F. M., D. Bodenstein, and R. C. King. 1965. Adipose tissue of Drosophila melanogaster. I. An experimental study of larval fat body. *J. Exp. Zool.* 158:141–153.
18. Nelliot, A., N. Bond, and D. K. Hoshizaki. 2006. Fat-body remodeling in Drosophila melanogaster. *Genesis.* 44:396–400.
19. Radulovic, M., O. Knittelfelder, …, S. D. Kohlwein. 2013. The emergence of lipid droplets in yeast: current status and experimental approaches. *Curr. Genet.* 59:231–242.
20. Kohlwein, S. D. 2010. Obese and anorexic yeasts: experimental models to understand the metabolic syndrome and lipotoxicity. *Biochim. Biophys. Acta.* 1801:222–229.
21. Cai, Y., J. M. Goodman, …, K. D. Chapman. 2015. Arabidopsis SEIPIN proteins modulate triacylglycerol accumulation and influence lipid droplet proliferation. *Plant Cell.* 27:2616–2636.
22. Herms, A., M. Bosch, …, A. Pol. 2013. Cell-to-cell heterogeneity in lipid droplets suggests a mechanism to reduce lipotoxicity. *Curr. Biol.* 23:1489–1496.
23. Hsieh, K., Y. K. Lee, …, A. R. Kimmel. 2012. Perilipin family members preferentially sequester to either triacylglycerol-specific or cholesteryl-ester-specific intracellular lipid storage droplets. *J. Cell Sci.* 125:4067–4076.
24. Corcoran, M. P., S. Lamon-Fava, and R. A. Fielding. 2007. Skeletal muscle lipid deposition and insulin resistance: effect of dietary fatty acids and exercise. *Am. J. Clin. Nutr.* 85:662–677.
25. Stein, D. T., B. E. Stevenson, …, J. D. McGarry. 1997. The insulinotropic potency of fatty acids is influenced profoundly by their chain length and degree of saturation. *J. Clin. Invest.* 100:398–403.
26. Nolan, C. J., and C. Z. Larter. 2009. Lipotoxicity: why do saturated fatty acids cause and monounsaturates protect against it? *J. Gastroenterol. Hepatol.* 24:703–706.
27. Seppänen-Laakso, T., I. Laakso, and R. Hiltunen. 2002. Analysis of fatty acids by gas chromatography, and its relevance to research on health and nutrition. *Anal. Chim. Acta.* 465:39–62.
28. Daemen, S., M. A. M. J. van Zandvoort, …, M. K. C. Hesselink. 2015. Microscopy tools for the investigation of intracellular lipid storage and dynamics. *Mol. Metab.* 5:153–163.
29. Anderson, J. L., J. D. Carten, and S. A. Farber. 2016. Using fluorescent lipids in live zebrafish larvae: from imaging whole animal physiology to subcellular lipid trafficking. *Methods Cell Biol.* 133:165–178.

30. Evans, C. L., and X. S. Xie. 2008. Coherent anti-stokes Raman scattering microscopy: chemical imaging for biology and medicine. *Annu. Rev. Anal. Chem. (Palo Alto, Calif.).* 1:883–909.

31. Yu, Y., P. V. Ramachandran, and M. C. Wang. 2014. Shedding new light on lipid functions with CARS and SRS microscopy. *Biochim. Biophys. Acta.* 1841:1120–1129.

32. Cheng, J. X., and X. S. Xie. 2015. Vibrational spectroscopic imaging of living systems: an emerging platform for biology and medicine. *Science.* 350:aaa8870.

33. Kompauer, M., S. Heiles, and B. Spengler. 2017. Atmospheric pressure MALDI mass spectrometry imaging of tissues and cells at 1.4-μm lateral resolution. *Nat. Methods.* 14:90–96.

34. Borisjuk, L., H. Rolletschek, and T. Neuberger. 2013. Nuclear magnetic resonance imaging of lipid in living plants. *Prog. Lipid Res.* 52:465–487.

35. Heymsfield, S. B., H. H. Hu, …, O. Carmichael. 2015. Emerging technologies and their applications in lipid compartment measurement. *Trends Endocrinol. Metab.* 26:688–698.

36. Hamilton, G., T. Yokoo, …, M. S. Middleton. 2011. In vivo characterization of the liver fat $^{1}$H MR spectrum. *NMR Biomed.* 24:784–790.

37. Syed, A., and E. A. Smith. 2017. Raman imaging in cell membranes, lipid-rich organelles, and lipid bilayers. *Annu. Rev. Anal. Chem. (Palo Alto, Calif.).* 10:271–291.

38. Camp, C. H., Jr., and M. T. Cicerone. 2015. Chemically sensitive bioimaging with coherent Raman scattering. *Nat. Photonics.* 9:295–305.

39. Rinia, H. A., K. N. Burger, …, M. Müller. 2008. Quantitative label-free imaging of lipid composition and packing of individual cellular lipid droplets using multiplex CARS microscopy. *Biophys. J.* 95:4908–4914.

40. Di Napoli, C., I. Pope, …, P. Borri. 2014. Hyperspectral and differential CARS microscopy for quantitative chemical imaging in human adipocytes. *Biomed. Opt. Express.* 5:1378–1390.

41. Wu, H., J. V. Volponi, …, S. Singh. 2011. In vivo lipidomics using single-cell Raman spectroscopy. *Proc. Natl. Acad. Sci. USA.* 108:3809–3814.

42. Schie, I. W., L. Nolte, …, T. Huser. 2013. Direct comparison of fatty acid ratios in single cellular lipid droplets as determined by comparative Raman spectroscopy and gas chromatography. *Analyst (Lond.).* 138:6662–6670.

43. Di Napoli, C., I. Pope, …, P. Borri. 2016. Quantitative spatiotemporal chemical profiling of individual lipid droplets by hyperspectral CARS microscopy in living human adipose-derived stem cells. *Anal. Chem.* 88:3677–3685.

44. El Hachmane, M. F., A. M. Komai, and C. S. Olofsson. 2015. Cooling reduces cAMP-stimulated exocytosis and adiponectin secretion at a Ca2+-dependent step in 3T3-L1 adipocytes. *PLoS One.* 10:e0119530.

45. Komai, A. M., C. Brännmark, …, C. S. Olofsson. 2014. PKA-independent cAMP stimulation of white adipocyte exocytosis and adipokine secretion: modulations by Ca2+ and ATP. *J. Physiol.* 592:5169–5186.

46. Beopoulos, A., J. Cescut, …, J. M. Nicaud. 2009. Yarrowia lipolytica as a model for bio-oil production. *Prog. Lipid Res.* 48:375–387.

47. Mayers, J. J., A. Ekman Nilsson, …, K. J. Flynn. 2017. Nutrients from anaerobic digestion effluents for cultivation of the microalga Nannochloropsis sp. — impact on growth, biochemical composition and the potential for cost and environmental impact savings. *Algal Res.* 26:275–286.

48. Billecke, N., G. Rago, …, S. H. Parekh. 2014. Chemical imaging of lipid droplets in muscle tissues using hyperspectral coherent Raman microscopy. *Histochem. Cell Biol.* 141:263–273.

49. Liu, Y., Y. J. Lee, and M. T. Cicerone. 2009. Fast extraction of resonant vibrational response from CARS spectra with arbitrary nonresonant background. *J. Raman Spectrosc.* 40:726–731.

50. Zhao, J., H. Lui, …, H. Zeng. 2007. Automated autofluorescence background subtraction algorithm for biomedical Raman spectroscopy. *Appl. Spectrosc.* 61:1225–1232.

51. Billecke, N., M. Bosma, …, S. H. Parekh. 2015. Perilipin 5 mediated lipid droplet remodelling revealed by coherent Raman imaging. *Integr. Biol.* 7:467–476.

52. Waschatko, G., N. Billecke, …, S. H. Parekh. 2016. Label-free in situ imaging of oil body dynamics and chemistry in germination. *J. R. Soc. Interface.* 13:20160677.

53. Cavonius, L., H. Fink, …, A. Enejder. 2015. Imaging of lipids in microalgae with coherent anti-stokes Raman scattering microscopy. *Plant Physiol.* 167:603–616.

54. Brackmann, C., J. Norbeck, …, A. Enejder. 2009. CARS microscopy of lipid stores in yeast: the impact of nutritional state and genetic background. *J. Raman Spectrosc.* 40:748–756.

55. Ohsaki, Y., M. Suzuki, and T. Fujimoto. 2014. Open questions in lipid droplet biology. *Chem. Biol.* 21:86–96.

56. Liu, B., and C. Benning. 2013. Lipid metabolism in microalgae distinguishes itself. *Curr. Opin. Biotechnol.* 24:300–309.

57. Mayers, J. J., K. J. Flynn, and R. J. Shields. 2014. Influence of the N:P supply ratio on biomass productivity and time-resolved changes in elemental and bulk biochemical composition of Nannochloropsis sp. *Bioresour. Technol.* 169:588–595.

58. Crown, S. B., N. Marze, and M. R. Antoniewicz. 2015. Catabolism of branched chain amino acids contributes significantly to synthesis of odd-chain and even-chain fatty acids in 3T3-L1 adipocytes. *PLoS One.* 10:e0145850.

59. Rizzatti, V., F. Boschi, …, M. Zamboni. 2013. Lipid droplets characterization in adipocyte differentiated 3T3-L1 cells: size and optical density distribution. *Eur. J. Histochem.* 57:e24.

60. Arisawa, K., I. Ichi, …, Y. Fujiwara. 2013. Changes in the phospholipid fatty acid composition of the lipid droplet during the differentiation of 3T3-L1 adipocytes. *J. Biochem.* 154:281–289.